

# Microcavity controlled coupling of excitonic qubits

F. Albert,<sup>1</sup> K. Sivalertporn,<sup>2</sup> J. Kasprzak,<sup>3</sup> M. Strauß,<sup>1</sup> C. Schneider,<sup>1</sup> S. Höfling,<sup>1</sup>  
M. Kamp,<sup>1</sup> A. Forchel,<sup>1</sup> S. Reitzenstein,<sup>1,\*</sup> E. A. Muljarov,<sup>2,†</sup> and W. Langbein<sup>2</sup>

<sup>1</sup>*Technische Physik, Physikalisches Institut, and Wilhelm Conrad Röntgen Research Center for Complex Material Systems, Universität Würzburg, Am Hubland, D-97074 Würzburg, Germany*

<sup>2</sup>*Cardiff University School of Physics and Astronomy, The Parade, Cardiff CF24 3AA, United Kingdom*

<sup>3</sup>*Institut Néel, CNRS et Université Joseph Fourier, BP 166, F-38042 Grenoble Cedex 9, France*  
(Dated: April 19, 2022)

Controlled non-local energy and coherence transfer enables light harvesting in photosynthesis and non-local logical operations in quantum computing. The most relevant mechanism of coherent coupling of distant qubits is coupling via the electromagnetic field. Here, we demonstrate the controlled coherent coupling of spatially separated excitonic qubits via the photon mode of a solid state microresonator. This is revealed by two-dimensional spectroscopy of the sample's coherent response, a sensitive and selective probe of the coherent coupling. The experimental results are quantitatively described by a rigorous theory of the cavity mediated coupling within a cluster of quantum dots excitons. Having demonstrated this mechanism, it can be used in extended coupling channels - sculptured, for instance, in photonic crystal cavities - to enable a long-range, non-local wiring up of individual emitters in solids.

Sunlight absorption via antenna proteins and the subsequent resonant energy transfer over a few nanometers towards the reaction centre is at the heart of the photosynthesis process<sup>1,2</sup>. In this case the electronic or Förster coupling strength and the local vibrational dissipation is tuned to achieve a fast directional energy transfer. Instead, in quantum information science and cavity quantum electrodynamics (cQED), the quantum bus technology aims to provide dissipation-less coupling between distant quantum systems. Within this field, long-range coherent coupling between individual, distant superconducting qubits has recently been demonstrated<sup>3</sup>, so that the construction of quantum logic gates and networks is within the reach of present technology<sup>4-6</sup>. In this context, qubits embedded in a solid state matrix are attractive, as they can fully benefit from the lithographic and materials processing techniques developed in the semiconductor industry to fabricate on-demand photonic layouts, so as to enable long-range coherent coupling within a discrete set of qubits via a photonic intra-cavity bus. Moreover, their “niche” with respect to superconducting qubits is marked out by a simultaneous functionality at relatively high temperatures and at optical frequencies, and they provide an interface to flying qubits such as photons in optical fibres.

In recent years, significant progress has been made in the realization of high quality optical microresonators which enabled pioneering demonstrations of the strong<sup>7-10</sup> and quantum strong coupling regime<sup>11,12</sup> in solid state. Micropillar cavities (cf. Fig. 1a) are a model system for the study of strong coupling in this field. They consist of self-assembled InGaAs quantum dots (QD) - providing individual exciton states (X) of high oscillator strength, located in the anti-node of the fundamental cavity mode (C). In these structures a quantum of optical excitation coherently oscillates between the fermionic exciton and bosonic cavity photon state. The resulting

eigenstates of mixed exciton and photon character form a Jaynes-Cummings (JC) ladder<sup>13</sup> with increasing number of photons in the cavity mode, showing a Rabi splitting of the rungs proportional to the root of the photon number.

In this Letter we report on coherent measurements and modeling of cavity-mediated coherent coupling between three quantum dot excitons, moving from the JC ladder to the Tavis-Cummings (TC) ladder<sup>14</sup>. This constitutes a crucial step towards a quantum bus based on semiconductor photonic structures.

Coherent photonic coupling of distant qubits is realized here by their dipole interaction with a common optical mode of a high-quality microresonator. For this purpose we have chosen a micropillar similar to that employed in Ref. 12 as described in the Methods section. By micro-photoluminescence ( $\mu$ PL) measurements as shown in Fig. 1b, we have identified a triplet of Xs - labeled X1, X2 and X3, which at a temperature of 8 K are slightly blue-shifted from the cavity. Increasing the sample temperature, the Xs (short-dashed lines) are tuned through C (long-dashed line) due to a reduction of the semiconductor band-gap. The data reveal three X-C avoided crossings at around 13 K, 21 K and 25 K, showing that each of them is in the strong coupling regime.

A triple exciton - cavity system has a level scheme as shown in Fig. 2, more complex than the previously studied single exciton-cavity system<sup>12</sup>. It hosts four polaritonic transitions from the vacuum state. The polariton frequency tuning (solid lines in Fig. 1b) as well as the variation of polariton linewidths (solid lines in Fig. 1c) can be described by a coupled oscillator model with the X1-C, X2-C, X3-C coupling parameters  $(g_1, g_2, g_3) = (43, 40, 31.5) \mu\text{eV}$ , homogeneous broadenings  $(\gamma_{X1}, \gamma_{X2}, \gamma_{X3}, \gamma_C) = (18, 11.5, 16, 36.5) \mu\text{eV}$ , and frequency distances  $\omega_{X2} - \omega_{X1} = 131 \mu\text{eV}$ ,  $\omega_{X3} - \omega_{X1} = 248 \mu\text{eV}$ . The parameters were obtained from a global fit of the coupled oscillator model to the detuning-

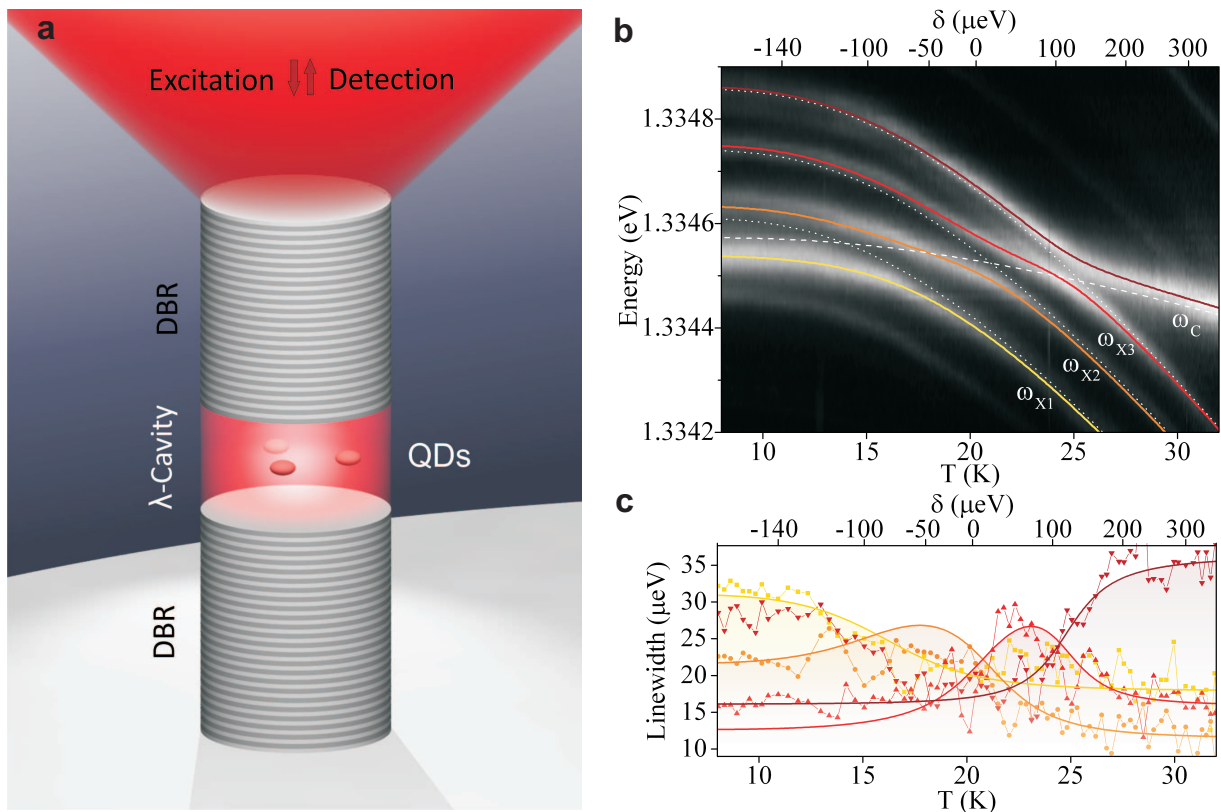


FIG. 1. Characterization of the investigated quantum dot - micropillar system. a) Sketch of the micropillar structure including the light coupling from the top facet. b) Temperature dependent photoluminescence spectral intensity under non-resonant excitation on a linear grey scale black (0) to white. The bare resonance energies of excitons and the cavity mode (white dotted and dashed lines, respectively), and the coupled polariton energies (solid lines) obtained from a Lorentzian lineshape fit and modelling (see supplementary material) are overlaid to the data. The corresponding average detuning  $\delta$  (see Eqn. 1) is shown on the upper axis scale. c) Coupled resonance linewidths (measured: symbols, modeling: lines). Colours and linestyles as in b).

dependent transition energies and broadenings determined by Lorentzian lineshape fitting of the  $\mu$ PL-spectra in Fig. 1b as described in the supplementary material (SM). To describe the detuning in this TC system with non-identical two-level systems, we introduce the average cavity detuning

$$\delta = \omega_C - \frac{\sum_{n=1}^3 g_n \omega_{Xn}}{\sum_{n=1}^3 g_n} \quad (1)$$

having the values of  $\delta = (-124, 16, 124) \mu\text{eV}$  at the three anti-crossing points and shown in the top axis of Fig. 1b. Multi-polaritonic features as reported in Fig. 1b,c were previously observed in  $\mu$ PL experiments<sup>15,16</sup> and indicate via an anti-crossing behaviour between individual excitons and the cavity mode that Xs could be coherently wired up by the cavity field. However, a direct measurement of coherent coupling is not afforded by  $\mu$ PL measuring the incoherent emission, neither does it provide means to perform coherent optical manipulation in prospective quantum bus nanophotonic structures. An explicit demonstration and selective manipulation of the cavity-mediated coherent coupling of excitons requires

extracting and controlling the coherent response of the photonic resonator.

To demonstrate and study the cavity mediated coherent coupling of Xs we employ here heterodyne spectral interferometry<sup>17</sup> (HSI) to detect the cavity-mediated coherent coupling between the excitons. This technique is used to measure the four-wave mixing (FWM) of the strongly-coupled Xs-C system, which arises from the optical nonlinearity of the quantum dot excitons. In short, two pulses  $E_1$  and  $E_2$  of 1 ps duration and variable delay  $\tau$  are exciting the fundamental cavity mode, see Fig. S6 in the SM. The resulting FWM polarization emitted from the micropillar  $P(t, \tau) \propto E_1^* E_2^2$  and its Fourier transform (FT) versus  $t$ ,  $\tilde{P}(\omega, \tau)$ , are measured using spectral interferometry.

The coherent dynamics giving rise to FWM involves the four Xs-C mixed states of the first rung of the TC ladder, which were identified in  $\mu$ PL, and additionally the 7 polariton states of the second rung which are mixed states of the family of uncoupled exciton-photon states of the second rung: one two-photon state without excitons, three one-photon states with one of the three excitons

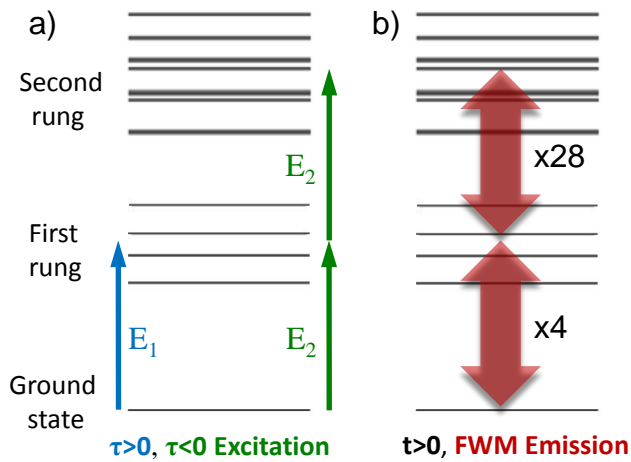


FIG. 2. Level scheme of the Tavis-Cummings ladder of the three exciton - one cavity system, and transitions relevant for the coherent FWM response, for  $\delta = -29 \mu\text{eV}$ . a) Coherence created by the pulse arriving first ( $E_1$  for  $\tau > 0$ ,  $E_2$  for  $\tau < 0$ ). b) Transitions emitting FWM after the arrival of the second pulse.

filled, and three zero-photon states with two of the three exciton states filled. A sketch of the resulting ladder of levels at  $T=19 \text{ K}$  ( $\delta = -29 \mu\text{eV}$ ) is shown in Fig. 2, together with the transitions relevant for the delay-time and real-time coherent dynamics probed in FWM. For positive delay  $\tau > 0$ , pulse  $E_1$  arrives first and creates a one-photon coherence given by a wavepacket of the 4 states of the first rung, which is coherently evolving until the arrival of  $E_2$ . Conversely, for negative delay  $\tau < 0$ , pulse  $E_2$  arrives first and creates a two-photon coherence given by a wavepacket in the second rung, which is coherently evolving until the arrival of  $E_1$ . In both cases, at the arrival of the second pulse FWM is created as a superposition of all optical transitions between the ground state, first and second rung, consisting of 4 transitions between the ground state and the first rung and 28 transitions between the first and second rung of the TC ladder. We calculate the FWM polarization analytically taking into account the states up to the second rung, by solving the master equation for the density matrix using a standard Xs-C coupling Hamiltonian and a Lindblad dissipation operator (see SM). This approach is exact for the third-order FWM signal of an initially unexcited system.

The resulting measurements and corresponding predictions of FWM of the system are given in Fig. 3 as function of time delay  $\tau$  for two different detuning parameters. For  $\delta = -29 \mu\text{eV}$  ( $T = 19 \text{ K}$ ), the spectrally resolved  $|\tilde{P}(\omega, \tau)|^2$  and time-resolved  $|P(t, \tau)|^2$  are shown in Figs. 3a,c, respectively. A dynamics significantly richer than in a single exciton case<sup>12</sup> is observed, as expected from the larger number of levels in the first and second rungs, providing 32 instead of 6 transitions contribut-

ing to the FWM (see Fig. 2). The time-integrated FWM power  $|P|_{\text{int}}^2(\tau) = \int |P(t, \tau)|^2 dt$  and the power  $|P(t_m, \tau)|^2$  at a given time  $t_m = 21 \text{ ps}$  corresponding to the build-up lag of the FWM in such strongly coupled exciton-cavity systems<sup>12</sup> are presented in Fig. 3e. On a qualitative level, we notice the FWM beat as a function of  $\tau$  with a period of about 17 ps, corresponding to a spectral splitting of  $243 \mu\text{eV}$ . This is much larger than the Rabi splitting of any individual X, and is close to the total splitting of  $2(g_1 + g_2 + g_3) = 229 \mu\text{eV}$ , indicating that all four polaritons contribute towards the coherent dynamics. In Figs. 3b,d we present the predicted FWM corresponding to 3a,c, using the exciton and cavity parameters retrieved from the  $\mu\text{PL}$  data (see Fig. 1 and the SM). The prediction, which takes into account the coherent evolution in the TC ladder shown in Fig. 2, reproduces the rich features of the measurements quantitatively.

Modifying the detuning, we can adjust the system to exhibit only one exciton in resonance with the cavity, while the other excitons are significantly detuned, so that the dynamics resembles that of a simpler single-exciton cavity system. This is achieved at  $\delta = -133 \mu\text{eV}$  ( $T=13.5 \text{ K}$ ), for which X1 is in resonance with C within  $5 \mu\text{eV}$ , whilst X2 and X3 are detuned by  $135 \mu\text{eV}$  and  $253 \mu\text{eV}$ , respectively. The measured and predicted  $|\tilde{P}(\omega, \tau)|^2$  and  $|P(t, \tau)|^2$  are presented in Fig. 3f,h and Fig. 3g,i, respectively, while the time-integrated FWM is displayed in Fig. 3j. We observe a beat versus delay  $\tau$  with a period of about 50 ps, corresponding to a polaritonic splitting of  $83 \mu\text{eV}$ , somewhat larger than the calculated splitting of  $60 \mu\text{eV}$ , which is slightly below  $2g_1$  due to the finite damping. The faster than expected beat period is due to remaining influence of the two additional excitons, as shown by the agreement of the predicted dynamics including all excitons (see solid line) with the measurements.

The agreement between the measured FWM dynamics and independently predicted FWM in the framework of the cavity-mediated coupling model for different detuning is revealing the coherent wiring up of the three Xs via the cavity mode in the studied microresonator. A definite display of the coherent coupling is afforded by the two-dimensional (2D) frequency domain representation of the FWM, in which coherent coupling is observed as off-diagonal signals<sup>1,2,18</sup>. We retrieve the 2D FWM<sup>17</sup> by Fourier-transforming  $\tilde{P}(\omega, \tau)$  from the delay time  $\tau$  into the conjugated frequency  $\omega_\tau$  yielding  $\bar{P}(\omega, \omega_\tau)$ . In this transformation we use only positive delays  $\tau > 0$ , such that  $\omega_\tau$  represents the frequency of the first-order polarization created by  $E_1$ . The resulting two-dimensional FWM diagrams  $\bar{P}(\omega, \omega_\tau)$  are presented in Fig. 4a,d. In this representation, coupled resonances manifest themselves by corresponding off-diagonal components, showing that resonances excited by the first pulse in first-order ( $\omega_\tau$  axis) coherently couple to a different resonances emitting in third-order ( $\omega$  axis). To enable the Fourier transformation we set the relative phase of data at different delays  $\tau$  using a phase correction<sup>19</sup> at a given  $\omega$  (see yel-

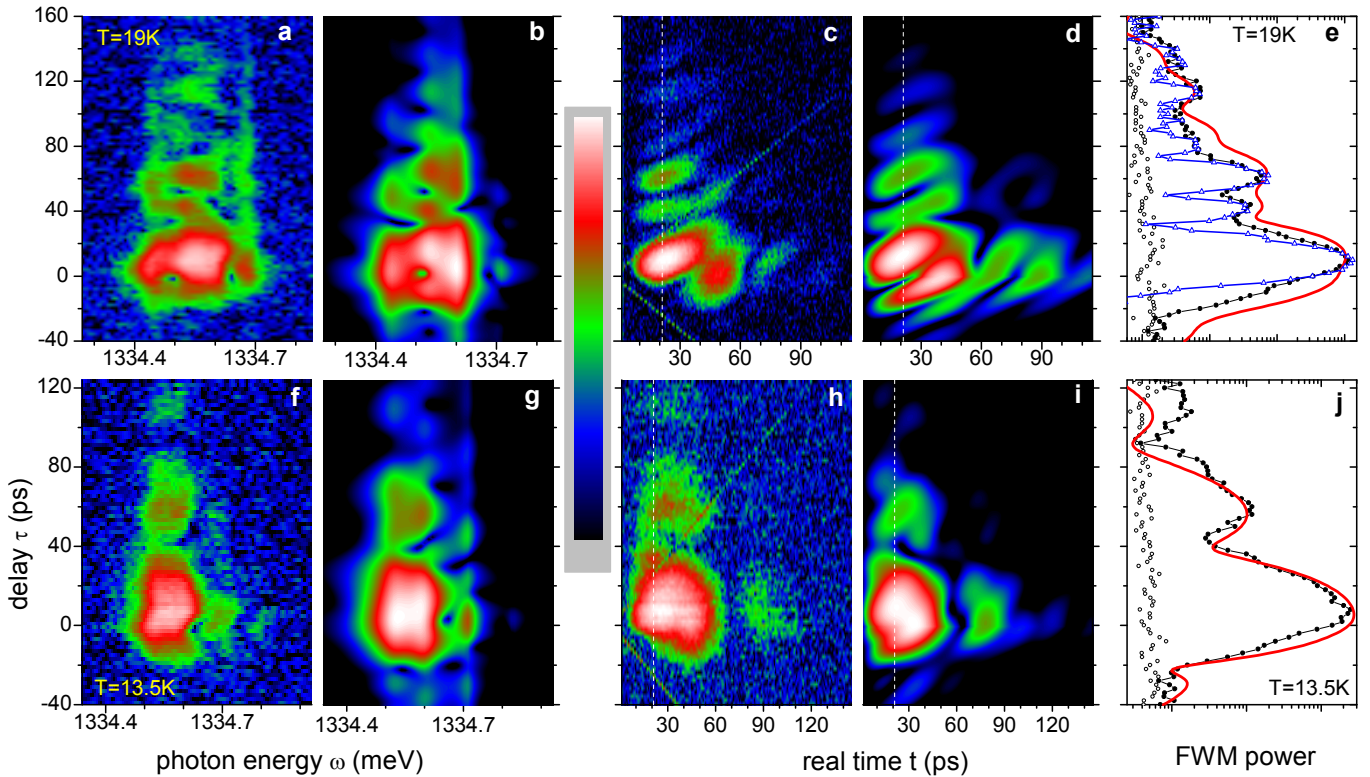


FIG. 3. Delay time dependence of coherent response for  $T = 19$  K (top) and  $T = 13.5$  K (bottom). Spectrally resolved FWM power  $|\tilde{P}(\omega, \tau)|^2$ , measured (a,f) and predicted (b,g), on a logarithmic colour scale over 4 orders of magnitude. Time-resolved FWM power  $|P(t, \tau)|^2$ , measured (c,h) and predicted (d,i), over 3 orders. (e,j) Time-integrated FWM power  $|P_{\text{int}}^2(\tau)|$ , measured (black circles) and predicted (red line), and measured  $|P(21 \text{ ps}, \tau)|^2$  (blue triangles). The noise of  $|P_{\text{int}}^2(\tau)|$  is given as open circles.

low arrows) as discussed in the SM. The effect of the phase-correction is illustrated in the difference between the predictions with and without phase correction given in Fig. 4b,c, respectively. The phase correction leads to a weighting in the first-order frequency, but does not qualitatively change the off-diagonal structure.

Due to the contributions of the 28 second-rung transitions, the features in 2D FWM are broadened. Post-selecting the FWM signal emitted after a survival time  $t_s$  after its creation by the second pulse at  $t = 0$ , resulting in the 2D FWM  $\tilde{P}_s(\omega, \omega_\tau, t_s)$ , we can suppress the fast decaying components<sup>12</sup>. The measured and predicted post-selected  $\tilde{P}_s(\omega, \omega_\tau, 42.5 \text{ ps})$  (see Fig. 4d,e,f) are dominated by the first-rung transitions and display a clear separation between the multiple off-diagonals at the polariton frequencies  $\lambda_{1,k}$  (see SM), showing cavity-mediated mutual coherent coupling between Xs. The corresponding data for  $T = 13.5$  K ( $\delta = -133 \mu\text{eV}$ ) given in the SM, Fig. S6, shows the coherent coupling between two polaritonic modes dominated by the cavity and X1. A detailed analysis of the strength of the off-diagonal peaks and their relation to the coherent coupling strength will be presented in a forthcoming work.

The observed coherent coupling between three qubits via the cavity mode demonstrates that an optical mi-

crocavity can act as a coupling bus for excitonic qubits. The coherent interaction can be controlled by non-local tuning of the cavity mode or the exciton energy, or by switching the excitonic qubit between bright and dark exciton states<sup>20</sup>. The coupling via the cavity mode has the prospect to be spatially extended in coupled cavity structures, for example in photonic crystals<sup>21</sup>. The small size of the quantum dots with respect to the cavity enables coupling of many more than three qubits, enhancing the prospects of quantum information processing on a chip with a photonic interface.

## Methods

**Samples:** The fabrication process of high-Q quantum dot micropillar structures starts with the growth of a planar microcavity on an undoped GaAs substrate by molecular beam epitaxy. A GaAs  $\lambda$ -cavity with a single layer of self-assembled  $\text{In}_{0.4}\text{Ga}_{0.6}\text{As}$  QDs with a ground state exciton emission wavelength around 930 nm is sandwiched between two distributed Bragg reflectors (DBR) providing a vertical photon confinement. The upper (lower) DBR consists of 26 (30) mirror pairs, which are made of  $\lambda/4$  layers of GaAs and AlAs. For lateral photon confinement micropillars



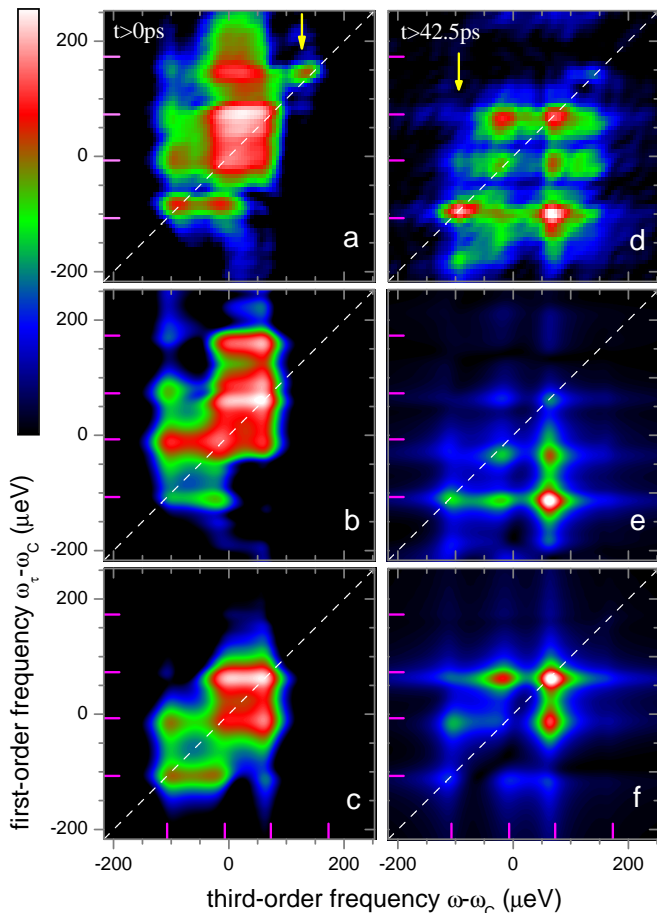


FIG. 4. Two-dimensional FWM at T=19 K. Power  $|\bar{P}(\omega, \omega_\tau)|^2$ , measured (a) and predicted with (b) and without (c) phase correction. Logarithmic colour scale from 0.09 (black) to 1 arbitrary units. Yellow arrows indicate the  $\omega$  of the phase correction. Magenta ticks indicate the polariton frequencies of the first rung  $\lambda_{1,k}$  (see SM). (d,e,f) as (a,b,c), but showing the post-selected  $|\bar{P}_s(\omega, \omega_\tau, 42.5 \text{ ps})|^2$  on a linear colour scale from 0.01 to 0.24 arbitrary units.

with a nominally circular cross-section and diameters between  $1.6 \mu\text{m}$  and  $2 \mu\text{m}$  were structured by means of high resolution electron beam lithography and electron cyclotron etching. The fundamental cavity mode in the investigated structure has a Q-factor of 30000, and a corresponding photon lifetime of about 10 ps within its mode volume of approximately  $0.3 \mu\text{m}^3$ .

**FWM experiment:** We employ heterodyne spectral interferometry<sup>17</sup>, using a pair of pulse trains,  $E_1$  and  $E_2$  at a repetition rate of 76 MHz and 1 ps pulse-duration which are frequency up-shifted by  $(\Omega_1/2\pi, \Omega_2/2\pi) = (79, 80.7) \text{ MHz}$  by acousto-optic devices. The spatial mode of  $E_1$  and  $E_2$  is matched to the cavity mode on the top facet of the micropillar by a

microscope objective mounted inside a helium bath cryostat. The pulses are resonant to the cavity mode and are injecting into the intra-cavity field in average 0.25 (0.75) photons per pulse of  $E_1$  ( $E_2$ ), respectively, see Fig. S7 in SM. The emitted light is interfered with a frequency unshifted reference field and the FWM signal is selected at the heterodyne beat note  $2\Omega_2 - \Omega_1$  and spectrally resolved. The complex FWM response  $P(t, \tau) \propto E_1^* E_2^2$  is retrieved by spectral interferometry<sup>17,22</sup>.

**Theory:** We use a standard approach<sup>15,16,23</sup>, with the Hamiltonian of a single photonic mode coupled to three two-level systems with dissipation of all components taken into account by a Lindblad super-operator. To calculate the FWM polarization, we follow our earlier rigorous approach<sup>12,24</sup> to the optical response of a system on a sequence of optical pulses. For the present system excited by two ultrashort pulses it has the analytic form

$$P_{\text{FWM}}(t, \tau) = \sum_{jk} c_{jk} e^{i\tilde{\omega}_j t} e^{i\lambda_k \tau} \quad (2)$$

in which  $\lambda_k = \lambda_{1k}^*$  ( $\lambda_k = \lambda_{2k}$ ) are the complex polariton frequencies of the first (second) rung, for positive (negative) delay times  $\tau$ , respectively, while  $\tilde{\omega}_j$  are the complex frequencies of all possible transitions between the ground state and the first rung and between the first and second rung, all contributing to the real-time dynamics.

The expansion coefficients  $c_{jk}$  are calculated exactly reducing the full master equation for the density matrix to a finite matrix problem. Further details are available in the SM.

## ACKNOWLEDGMENTS

F.A. acknowledges support by the Deutscher Akademischer Austauschdienst under project number 50743470. The work was in part supported by the Deutsche Forschungsgemeinschaft through the research group ‘Quantum Optics in Semiconductor Nanostructures’ and the State of Bavaria. K.S. acknowledges support by the Royal Thai Government.

**Author contributions:** The work was initiated by SR and WL. The sample was grown and processed by SR, CK, CS, MS, SH and AF, and characterized by FA and SR. Measurements were performed by FA, JK, and WL, and analyzed by FA, JK, WL and EM. The theory was developed and compared with the experiment by KS, EM and WL. The manuscript was written by FA, JK, SR, EM, and WL.

The authors declare no competing financial interests.

- 
- \* Present Address: Institut für Festkörperphysik, Technische Universität Berlin, Hardenbergstrasse 36, 10623 Berlin, Germany
- † On leave from General Physics Institute RAS, Moscow, Russia
- <sup>1</sup> E. Collini, C. Y. Wong, K. E. Wilk, P. M. G. Curmi, P. Brumer, and G. D. Scholes, *Nature*, **463**, 644 (2010).
  - <sup>2</sup> G. D. Scholes, G. R. Fleming, A. Olaya-Castro, and R. van Grondelle, *Nature Chem.*, **3**, 763 (2011).
  - <sup>3</sup> J. Majer, J. M. Chow, J. M. Gambetta, J. Koch, B. R. Johnson, J. A. Schreier, L. Frunzio, D. I. Schuster, A. A. Houck, A. Wallraff, A. Blais, M. H. Devoret, S. M. Girvin, and R. J. Schoelkopf, *Nature*, **449**, 443 (2007).
  - <sup>4</sup> R. J. Schoelkopf and S. M. Girvin, *Nature*, **451**, 664 (2008).
  - <sup>5</sup> P. J. Leek, S. Filipp, P. Maurer, M. Baur, R. Bianchetti, J. M. Fink, M. Göppl, L. Steffen, and A. Wallraff, *Phys. Rev. B*, **79**, 180511(R) (2009).
  - <sup>6</sup> J. M. Chow, A. D. Córcoles, J. M. Gambetta, C. Rigetti, B. R. Johnson, J. A. Smolin, J. R. Rozen, G. A. Keefe, M. B. Rothwell, M. B. Ketchen, and M. Steffen, *Phys. Rev. Lett.*, **107**, 080502 (2011).
  - <sup>7</sup> J. P. Reithmaier, G. Şek, A. Löffler, C. Hoffmann, S. Kuhn, S. Reitzenstein, L. V. Keldysh, V. D. Kulakovskii, T. L. Reinecke, and A. Forchel, *Nature*, **432**, 197 (2004).
  - <sup>8</sup> T. Yoshie, A. Scherer, J. Hendrickson, G. Khitrova, H. M. Gibbs, G. Rupper, C. Ell, O. B. Shchekin, and D. G. Deppe, *Nature*, **432**, 200 (2004).
  - <sup>9</sup> E. Peter, P. Senellart, D. Martrou, A. Lemaître, J. Hours, J. M. Gérard, and J. Bloch, *Phys. Rev. Lett.*, **95**, 067401 (2005).
  - <sup>10</sup> R. Ohta, Y. Ota, M. Nomura, N. Kumagai, S. Ishida, S. Iwamoto, and Y. Arakawa, *Appl. Phys. Lett.*, **98**, 173104 (2011).
  - <sup>11</sup> A. Faraon, I. Fushman, D. Englund, N. Stoltz, P. Petroff, and J. Vuckovic, *Nature Physics*, **4**, 859 (2008).
  - <sup>12</sup> J. Kasprzak, S. Reitzenstein, E. A. Muljarov, C. Kistner, C. Schneider, M. Strauss, S. Höfling, A. Forchel, and W. Langbein, *Nature Materials*, **9**, 304 (2010).
  - <sup>13</sup> E. Jaynes and F. Cummings, *Proc. IEEE*, **51**, 89 (1963).
  - <sup>14</sup> M. Tavis and F. W. Cummings, *Phys. Rev.*, **170**, 379 (1968).
  - <sup>15</sup> S. Reitzenstein, A. Löffler, C. Hofmann, A. Kubanek, M. Kamp, J. P. Reithmaier, A. Forchel, V. D. Kulakovskii, L. V. Keldysh, I. V. Ponomarev, and T. L. Reinecke, *Optics Letters*, **31**, 1738 (2006).
  - <sup>16</sup> A. Laucht, J. M. Villas-Bôas, S. Stobbe, N. Hauke, F. Hofbauer, G. Böhm, P. Lodahl, M.-C. Amann, M. Kaniber, and J. J. Finley, *Phys. Rev. B*, **82**, 075305 (2010).
  - <sup>17</sup> W. Langbein and B. Patton, *Optics Letters*, **31**, 1151 (2006).
  - <sup>18</sup> S. Mukamel, *Annu. Rev. Phys. Chem.*, **51**, 691 (2000).
  - <sup>19</sup> J. Kasprzak, B. Patton, V. Savona, and W. Langbein, *Nature Photonics*, **5**, 57 (2011).
  - <sup>20</sup> E. Poem, Y. Kodriano, C. Tradonsky, N. H. Lindner, B. D. Gerardot, P. M. Petroff, and D. Gershoni, *Nature Physics*, **6**, 993 (2010).
  - <sup>21</sup> D. Englund, A. Faraon, B. Zhang, Y. Yamamoto, and J. Vučković, *Opt. Express*, **15**, 5550 (2007).
  - <sup>22</sup> W. Langbein and B. Patton, *J. Phys.: Condens. Matter*, **19**, 295203 (2007).
  - <sup>23</sup> F. P. Laussy, A. Laucht, E. del Valle, J. J. Finley, and J. M. Villas-Bôas, *Phys. Rev. B*, **84**, 195313 (2011).
  - <sup>24</sup> E. A. Muljarov and R. Zimmermann, *physica status solidi (b)*, **243**, 2252 (2006).

## Microcavity controlled coupling of excitonic qubits

F. Albert,<sup>1</sup> K. Sivalertporn,<sup>2</sup> J. Kasprzak,<sup>3</sup> M. Strauß,<sup>1</sup> C. Schneider,<sup>1</sup> S. Höfling,<sup>1</sup>  
M. Kamp,<sup>1</sup> A. Forchel,<sup>1</sup> S. Reitzenstein,<sup>1,\*</sup> E. A. Muljarov,<sup>2</sup> and W. Langbein<sup>2</sup>

<sup>1</sup>*Technische Physik, Physikalisches Institut, Universität Würzburg and  
Wilhelm Conrad Röntgen Research Center for Complex Material Systems,  
Am Hubland, D-97074 Würzburg, Germany*

<sup>2</sup>*Cardiff University School of Physics and Astronomy,  
The Parade, Cardiff CF24 3AA, United Kingdom*

<sup>3</sup>*Institut Néel, CNRS et Université Joseph Fourier,  
BP 166, F-38042 Grenoble Cedex 9, France*

(Dated: April 19, 2022)

### I. FOUR-WAVE MIXING RESPONSE OF $N$ QUANTUM DOTS COUPLED TO THE CAVITY

The Tavis-Cummings (TC) model of  $N$  quantum dots (QDs) coupled to a single photonic mode in a microcavity is described by the Hamiltonian

$$H = \omega_C a^\dagger a + \sum_{n=1}^N \left[ \omega_{X_n} |n\rangle \langle n| + g_n \left( a^\dagger |0\rangle \langle n| + a |n\rangle \langle 0| \right) \right], \quad (1)$$

in which  $\omega_C$  is the frequency of the cavity mode,  $\omega_{X_n}$  is exciton transition energy of the  $n$ -th QD, and  $g_n$  is the coupling strength between the  $n$ -th QD excitation and the cavity mode. Furthermore  $a^\dagger$  ( $a$ ) is the cavity photon creation (destruction) operator,  $|0\rangle$  is the ground state (GS) of the exciton system, and  $|n\rangle$  denotes the state with one exciton in the  $n$ -th QD and all other QDs empty. We use  $\hbar = 1$  for simplicity of notations. We assume that all QD excitons are close to resonance with the cavity mode, and neglect any excited or multi-excitonic states within the same QD, as they are generally off resonance. However, since we consider QDs which are electronically uncoupled, multi-excitonic states in which all excitons are in different QDs stay close to resonance with the cavity mode, and significantly contribute to the four-wave mixing (FWM) dynamics.

The system of the  $N$  QD excitons coupled to the cavity is excited by an external electric field consisting of two ultrashort pulses separated by the delay time  $\tau$  and having complex pulse areas  $\mu E_1$  and  $\mu E_2$ , where  $\mu$  is the effective dipole moment of the cavity mode. The measured FWM polarization is a third-order signal proportional to  $E_1^* E_2^2$ . In the calculation, the effect of the pulses is taken into account as follows. The first pulse  $E_1$  contributes in first-order, changing the density matrix according to

$$\rho^{(+)} = -i\mu E_1^* [a, \rho^{(-)}], \quad (2)$$

where  $\rho^{(-)}$  ( $\rho^{(+)}$ ) is the density matrix before (after) the pulse. The second pulse  $E_2$  contributing in second order results in the following change of the density matrix:

$$\rho^{(+)} = \frac{(-i)^2}{2} \mu^2 E_2^2 [a^\dagger, [a^\dagger, \rho^{(-)}]]. \quad (3)$$

Between and after the pulses the time evolution of the density matrix  $\rho(t)$  is described by the master equation

$$i \frac{d\rho}{dt} = \hat{L}\rho, \quad (4)$$

where  $\hat{L}$  is the Lindblad super-operator of the exciton-cavity system,

$$\hat{L}\rho = [H, \rho] - i\gamma_C (a^\dagger a \rho + \rho a^\dagger a - 2a \rho a^\dagger) + \sum_{n=1}^N \gamma_{X_n} \left[ |n\rangle \langle n| \rho + \rho |n\rangle \langle n| - 2|0\rangle \langle n| \rho |n\rangle \langle 0| \right], \quad (5)$$

with  $\gamma_C$  and  $\gamma_{X_n}$  being, respectively, the cavity damping and the exciton dephasing, which are assumed to be lifetime limited. Equation (4) has the following formal solution

$$\rho(t) = e^{-i\hat{L}(t-t')} \rho(t'), \quad (6)$$

and thus the FWM polarization takes the form

$$P(t, \tau) = \text{Tr}\{\rho a\} = \frac{(-i)^3}{2} \mu^3 E_1^* E_2^2 \cdot \text{Tr}\{R(t, \tau) a\} \quad (7)$$

where the third-order component of the density matrix is proportional to

$$R(t, \tau) = e^{-i\hat{L}t} \left[ a^\dagger, [a^\dagger, e^{-i\hat{L}\tau} [a, \rho(-\infty)]] \right], \quad (8)$$

for positive delay between the pulses ( $\tau > 0$ ), and to

$$R(t, \tau) = e^{-i\hat{L}t} \left[ a, e^{i\hat{L}\tau} [a^\dagger, [a^\dagger, \rho(-\infty)]] \right], \quad (9)$$

for negative delay ( $\tau < 0$ ). Here  $\rho(-\infty)$  is the density matrix before the excitation.

We solve equations (2)–(4) *exactly* by expanding all operators into a set of uncoupled exciton-photon states  $|i\rangle \equiv |n_{X1}, n_{X2}, \dots, n_{XN}; n_C\rangle$  ( $i = 0, 1, 2, \dots$ ), where  $n_{Xn} = 0, 1$  and  $n_C = 0, 1, 2, \dots$  are, respectively, the exciton and photon occupation numbers. We assume that the system is initially in its ground state, with the density matrix  $\rho(-\infty) = |\theta\rangle\langle\theta|$ . This is justified by the excitations of the system having an energy about 3 orders of magnitude larger than the thermal energy and coherence times shorter than the period of the repetitive excitation (13 ns) used in this work. The resulting FWM dynamics includes only transitions between the GS, the first rung, and the second rung of the TC ladder. With  $N$  quantum dots coupled to the cavity, there are  $N_1 = 1 + N$  states in the first rung and  $N_2 = 1 + N(N + 1)/2$  states in the second rung, so that the expansion of density matrix has the form

$$\rho(t) = \sum_{i,j=0}^{N_1+N_2} \rho_{ij}(t) |i\rangle\langle j|, \quad (10)$$

with  $1 + N_1 + N_2$  basis states. A similar expansion is used for the photon creation (annihilation) operator contributing to Eqs. (2) and (3). To solve the master equation (4) after the pulsed excitation, a bigger,  $M \times M$  matrix of the super-operator  $\hat{L}$  is introduced, with  $M = N_1(1 + N_2)$  being the total number of all possible transitions, between the GS and the first rung ( $N_1$ ), and between the first and second rungs ( $N_1 N_2$ ). Only such transitions contribute to the FWM polarization. The solution to Eq. (4) then has the matrix form

$$\rho(t) = e^{-i\hat{L}t} \rho(0) = \hat{U} e^{-i\hat{\Omega}t} \hat{V} \rho(0), \quad (11)$$

in which the matrix  $\hat{L}$  is diagonalised as

$$\hat{L} = \hat{U} \hat{\Omega} \hat{V}, \quad \hat{U} \hat{V} = \hat{1}, \quad (12)$$

with  $\hat{U}$  and  $\hat{V}$  being matrices of right and left eigenvectors and  $\hat{\Omega}$  a diagonal matrix of complex eigenfrequencies  $\tilde{\omega}_j$  of all possible transitions involved. The density matrix then becomes a finite superposition of exponentials,

$$\rho(t) = \sum_{j=1}^M r_j e^{-i\tilde{\omega}_j t} \quad (13)$$

with the frequencies  $\tilde{\omega}_j$  and matrices  $r_j$  calculated exactly. In particular,

$$\tilde{\omega}_j = \lambda_{1,k} \quad \text{and} \quad \tilde{\omega}_j = \lambda_{2,k} - \lambda_{1,m}^* \quad (14)$$

for the GS–first rung and first rung–second rung transitions, respectively, where  $\lambda_{1,k}$  ( $\lambda_{2,k}$ ) are the complex energy levels of the first (second) rung, calculated by diagonalizing of the complex symmetric matrix of a non-Hermitian Hamiltonian (see below). The time evolution between pulses is given by a smaller matrix  $\hat{L}$  as only transitions from the GS to the first (second) rung participate in the delay dynamics, for positive (negative) delay times. The FWM polarization then takes the following explicit form:

$$P(t, \tau) = \sum_{j=1}^M e^{i\tilde{\omega}_j t} \times \begin{cases} \sum_{k=1}^{N_1} a_{jk} e^{i\lambda_{1,k}^* \tau} & \tau > 0 \\ \sum_{k=1}^{N_2} b_{jk} e^{i\lambda_{2,k} \tau} & \tau < 0 \end{cases} \quad (15)$$



With the analytic form Eq. (15) at hand, it is straightforward to calculate the Fourier transform (FT) of the FWM polarization. In particular, for positive delays, its two-dimensional FT has the form

$$P(\omega, \omega_\tau) = \sum_{j=1}^M \sum_{k=1}^{N_1} \frac{a_{jk}}{(\omega - \tilde{\omega}_j + i\gamma_S)(\omega_\tau + \lambda_{1,k}^*)}, \quad (16)$$

where a Lorentzian spectrometer resolution  $\gamma_S$  (half width at half maximum) is included.

Although our analytical approach is general and can be used for any arbitrary  $N$  producing a reasonable size of the basis (the size of the matrix  $\hat{L}$  scales as  $N^3$ ), in the present calculation we concentrate on a system of  $N = 3$  QDs coupled to the cavity. Then the basis reduces to the following *twelve* states which include  $N_1 = 4$  states of first rung and  $N_2 = 7$  states of the second rung:

Ground state  $|0\rangle = |0, 0, 0; 0\rangle$ ;

First rung  $|1\rangle = |0, 0, 0; 1\rangle$ ,  $|2\rangle = |1, 0, 0; 0\rangle$ ,  $|3\rangle = |0, 1, 0; 0\rangle$ ,  $|4\rangle = |0, 0, 1; 0\rangle$ ;

Second rung  $|5\rangle = |0, 0, 0; 2\rangle$ ,  $|6\rangle = |1, 0, 0; 1\rangle$ ,  $|7\rangle = |0, 1, 0; 1\rangle$ ,  $|8\rangle = |0, 0, 1; 1\rangle$ ,  
 $|9\rangle = |1, 1, 0; 0\rangle$ ,  $|10\rangle = |1, 0, 1; 0\rangle$ ,  $|11\rangle = |0, 1, 1; 0\rangle$ . (17)

Both the density matrix and the photon creation operator are  $12 \times 12$  matrices, while the super-operator  $\hat{L}$  after the excitation by both pulses is represented by a  $32 \times 32$  matrix which is due to  $M = 32$  transitions: 4 transitions between the GS and the first rung and  $4 \times 7 = 28$  transitions between the first and second rungs.

The energy levels  $\lambda_{n,k}$  of the TC ladder are calculated by diagonalizing the effective non-Hermitian Hamiltonian:

$$\tilde{H} = \begin{pmatrix} \tilde{H}_1 & 0 & 0 & \dots \\ 0 & \tilde{H}_2 & 0 & \dots \\ 0 & 0 & \tilde{H}_3 & \dots \\ \vdots & \vdots & \vdots & \ddots \end{pmatrix}. \quad (18)$$

The first two blocks on the main diagonal of  $\tilde{H}$  refer to the first and second rungs, respectively:

$$\tilde{H}_1 = \begin{pmatrix} \tilde{\omega}_C & g_1 & g_2 & g_3 \\ g_1 & \tilde{\omega}_{X1} & 0 & 0 \\ g_2 & 0 & \tilde{\omega}_{X2} & 0 \\ g_3 & 0 & 0 & \tilde{\omega}_{X3} \end{pmatrix}, \quad (19)$$

$$\tilde{H}_2 = \begin{pmatrix} 2\tilde{\omega}_C & \sqrt{2}g_1 & \sqrt{2}g_2 & \sqrt{2}g_3 & 0 & 0 & 0 \\ \sqrt{2}g_1 & \tilde{\omega}_C + \tilde{\omega}_{X1} & 0 & 0 & g_2 & g_3 & 0 \\ \sqrt{2}g_2 & 0 & \tilde{\omega}_C + \tilde{\omega}_{X2} & 0 & g_1 & 0 & g_3 \\ \sqrt{2}g_3 & 0 & 0 & \tilde{\omega}_C + \tilde{\omega}_{X3} & 0 & g_1 & g_2 \\ 0 & g_2 & g_1 & 0 & \tilde{\omega}_{X1} + \tilde{\omega}_{X2} & 0 & 0 \\ 0 & g_3 & 0 & g_1 & 0 & \tilde{\omega}_{X1} + \tilde{\omega}_{X3} & 0 \\ 0 & 0 & g_3 & g_2 & 0 & 0 & \tilde{\omega}_{X2} + \tilde{\omega}_{X3} \end{pmatrix}, \quad (20)$$

where  $\tilde{\omega}_C = \omega_C - i\gamma_C$  and  $\tilde{\omega}_{Xn} = \omega_{Xn} - i\gamma_{Xn}$ .

## II. PHOTOLUMINESCENCE CHARACTERIZATION

The investigated sample consists of fields of 6 by 6 micropillars of nominally equal diameter, with  $50 \mu\text{m}$  separation in  $x$  and  $y$  direction corresponding to the  $[110]$  and  $[\bar{1}\bar{1}0]$  crystallographic directions of the GaAs substrate, respectively. Each micropillar was accompanied by a reference pillar of  $10 \mu\text{m}$  diameter at  $10 \mu\text{m}$  distance which was used to reflect the reference beam in the heterodyne spectral interferometry (HSI) experiment. A scanning electron microscopy image of a row is shown in Fig. S1a.

The micropillars have diameters of 1.5, 1.6, 1.7, 1.8 and  $1.9 \mu\text{m}$ , and for each diameter 10 equal fields provided 360 nominally equal micropillars. The sample was mounted on an  $x - y$  stage in a helium

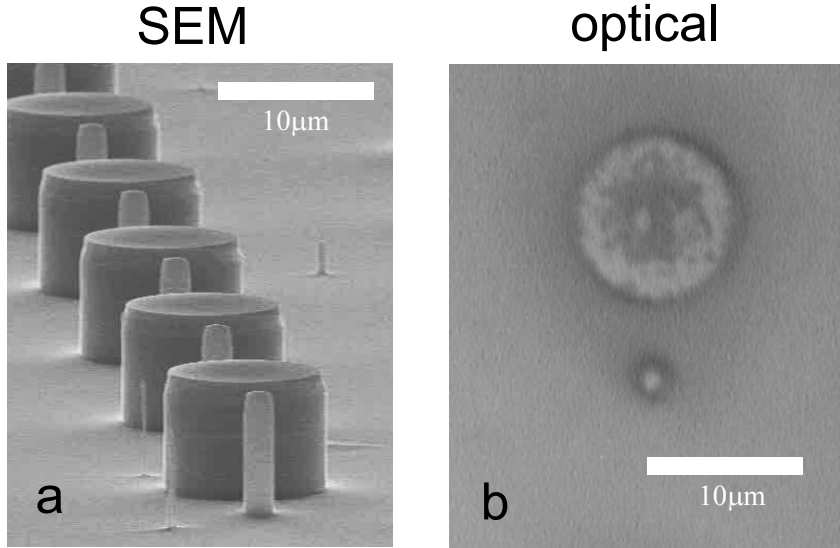


FIG. S1. Images of the investigated sample. a) Scanning electron microscopy image of a row of micropillar - reference pillar pairs. b) White light reflection image taken in the cryostat at 10 K using the same optical setup as in the confocal PL and HSI experiments. Scale bars are given.

bath cryostat, together with a microscope objective of 0.85 numerical aperture which was adjustable in all three dimensions by a home-build stage using piezoelectric bender actuators. A reflection image of a micropillar taken with this arrangement is shown in Fig. S1b. To identify micropillars in the strong coupling regime, we used confocal photoluminescence ( $\mu$ PL) excited by a laser of 532 nm wavelength, focussed to a spot of about  $0.5 \mu\text{m}$  FWHM on the top face of the micropillar. Typically 10% of the micropillars with  $1.5 - 1.7 \mu\text{m}$  diameter showed strong coupling. The micropillar presented in this work was selected from about 200 micropillars with the strongest coupling of multiple quantum dots. The photoluminescence excitation power at the micropillar was about 100 nW. At lower intensities the PL spectrum remained essentially unchanged, while at higher intensities line broadening and reduction of the Rabi-splitting was observed.

To characterize the quantum dot - cavity coupling,  $\mu$ PL spectra were measured as function of the sample temperature from 7 K to 35 K. The PL spectrum at each temperature was fitted by a sum of Lorentzian lines, as exemplified in Fig. S2. The resulting line positions as function of temperature were fitted with the first rung transition energies  $\lambda_{1,k}$  given by Eq.(19). In the fit, we used an explicit functional dependence for the temperature-tuning of the energies of quantum dots and cavity, from a model of the band-gap shift of semiconductors<sup>1</sup>.

$$\omega_{X_n}(T) = \omega_{X_n}(0) + F(T), \quad \omega_C(T) = \omega_C(0) + \eta F(T) \quad (21)$$

with

$$F(T) = -\frac{\alpha\theta}{2} \left( \coth\left(\frac{\theta}{2T}\right) - 1 \right) \quad (22)$$

The parameters describing the temperature-dependence were determined from a fit to the emission of quantum dots detuned from the cavity by more than 1 meV, yielding  $\alpha = (60.9 \pm 0.6) \mu\text{eV/K}$  and  $\theta = (58.9 \pm 1.0) \text{K}$ . The quoted errors represent the statistical variation of the results between different fitted quantum dots.

From the fit of  $\lambda_{1,k}$  to the measured line positions and widths, we deduce the low temperature energies  $\omega_{X_n}(0), \omega_C(0)$ , the linewidths  $\gamma_{X_n}, \gamma_C$  and the coupling strengths  $g_n$ , as shown in table I. Additionally, the scaling factor  $\eta = 0.227 \pm 0.003$ , for the cavity shift was determined, showing that the cavity shift is about 4 times less than the quantum dot exciton shift.

For simplicity, we assume here that the linewidths and the coupling strengths are independent of temperature, and that the linewidths are Lorentzian, i.e. homogeneously broadened. A spectrometer resolution of  $\gamma_S = 4 \mu\text{eV}$  (HWHM) was subtracted from the fitted linewidths.

The intrinsic homogeneous linewidth of the quantum dots<sup>2</sup> is expected to be limited by radiative decay and phonon scattering. The radiative decay time of the quantum dots in bulk GaAs is about

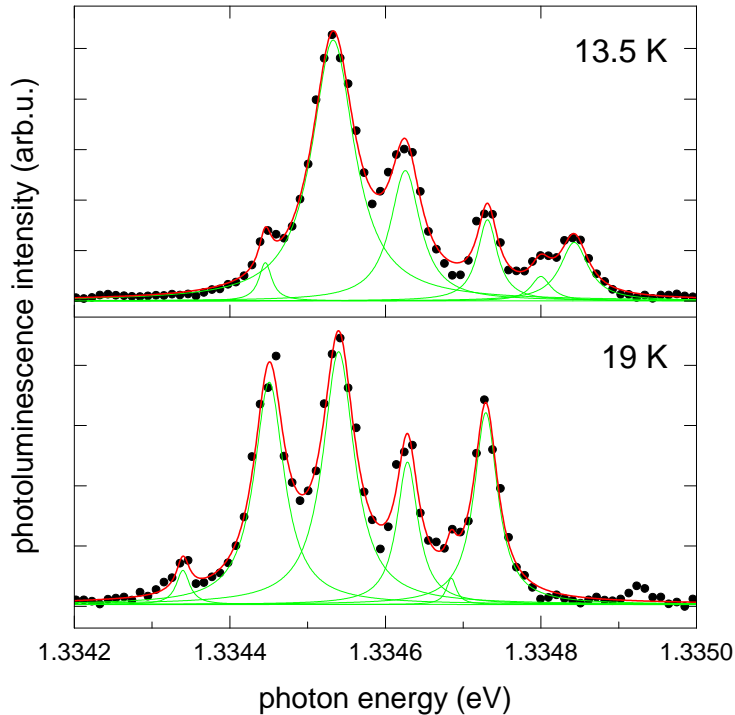


FIG. S2. Photoluminescence spectra from the investigated micropillar at a temperature of 13.5 K (top) and 19 K (bottom), and fits by multiple Lorentzian lines (solid lines).

parameter	value	unit
$\omega_{X1}(0)$	1.3346106	eV
$\omega_{X2}(0)$	1.3347412	eV
$\omega_{X3}(0)$	1.3348584	eV
$\omega_C(0)$	1.3345732	eV
$g_1$	43	$\mu\text{eV}$
$g_2$	40	$\mu\text{eV}$
$g_3$	31.5	$\mu\text{eV}$
$\gamma_{X1}$	18	$\mu\text{eV}$
$\gamma_{X2}$	11.5	$\mu\text{eV}$
$\gamma_{X3}$	16	$\mu\text{eV}$
$\gamma_C$	36.5	$\mu\text{eV}$

TABLE I. Parameters of the three-exciton cavity system deduced from a fit to the temperature-dependent photoluminescence spectra.

400 ps, corresponding to  $1 \mu\text{eV}$  HWHM. In micropillars, this decay is not significantly modified due to the presence of leaky modes which have a similar local density of states as the bulk modes<sup>3</sup>. The phonon-scattering increases the zero-phonon linewidth for quantum dots with 140 meV confinement energy<sup>2</sup> by about  $0.5 \mu\text{eV}$  at 20 K and  $2 \mu\text{eV}$  at 30 K.

The measured linewidths of different uncoupled quantum dots are between 10 and  $30 \mu\text{eV}$ , and vary from dot to dot, both in terms of low-temperature linewidth and dependence on temperature, which we attribute to spectral diffusion. Such a broadening mechanism is presently not taken into account in the FWM modeling, and might explain some of the remaining differences between the experimental data and the modeling, specifically for negative delay due to the expected photon echo formation. We plan to extend the modeling to include also inhomogeneous broadening and pure dephasing of the quantum dot excitons<sup>4,5</sup> in future work.

The coupling strength is expected to decrease with temperature proportional to the square root of the zero-phonon line weight<sup>2</sup>, resulting in a reduction of about 5% from 8 K to 30 K. We have neglected this dependence. The resulting fit (see Fig. 1) reproduces the energy positions and linewidths to within

the measurement error of about  $5 \mu\text{eV}$ . The above approximations are therefore reasonable for the data at hand. The linewidths of the strongly coupled modes are actually dominated by the cavity linewidth, which is given by the photon lifetime and thus Lorentzian. This reduces the importance of the broadening mechanism in the quantum dot excitons.

### III. POLARITON STATES

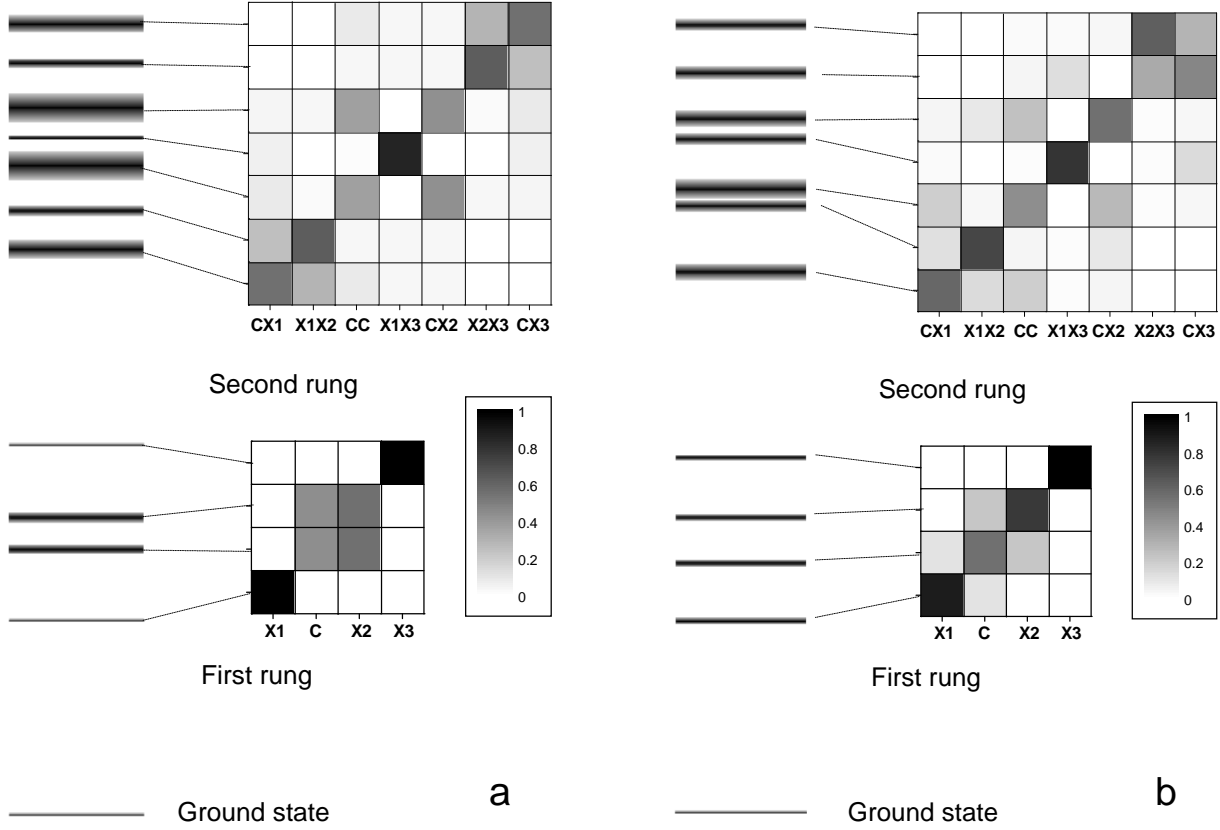


FIG. S3. Energies and linewidths of the polariton states of the first and second rungs and their probability distribution (grey scale matrices) in the basis of the uncoupled states Eq. (17) of the exciton-cavity system, calculated for (a) model symmetric structure and (b) realistic asymmetric structure with  $\delta = -29 \mu\text{eV}$  (corresponding to  $T = 19 \text{ K}$ ). The parameters of the system used for the symmetric structure are  $g_n = 40 \mu\text{eV}$ ,  $\gamma_{X_n} = 0$ ,  $\gamma_C = 60 \mu\text{eV}$ ,  $\omega_{X2} = \omega_C$ , and  $\omega_{X2} - \omega_{X1} = \omega_{X3} - \omega_{X2} = 130 \mu\text{eV}$  (corresponding to zero detuning). The parameters of the realistic structure are given in the main text and table I. Here, the similar contributions of the cavity mode to all states results in similar linewidths of the levels of a given rung.

The polariton states in the micropillar calculated for a symmetric model structure and realistic parameters of the investigated sample are shown in Fig. S3. The detuning dependence of the cavity and exciton levels are shown in Fig. S4.

### IV. SUPPLEMENTARY FWM RESULTS

Here we show supporting experimental and theoretical results concerning the four-wave mixing. Adding to the data shown in Figs. 3,4 of the main manuscript, we show here the calculated FWM dynamics for various detunings in Fig. S5, both the real-time resolved  $|P(t, \tau)|^2$ , the frequency resolved  $|\tilde{P}(\omega, \tau)|^2$ , and the 2D FWM  $|\tilde{P}(\omega, \omega_\tau)|^2$ .

The phase correction applied to the experimental FWM polarization  $\tilde{P}(\omega, \tau)$  setting the phase evolution of the FWM versus  $\tau$  to its expected evolution for an uncoupled system, is given by

$$\tilde{P}_{\text{cor}}(\omega, \tau) = \tilde{P}(\omega, \tau) \exp \left( i \left( \omega_{\text{cor}} \tau - \arg \tilde{P}(\omega_{\text{cor}}, \tau) \right) \right). \quad (23)$$

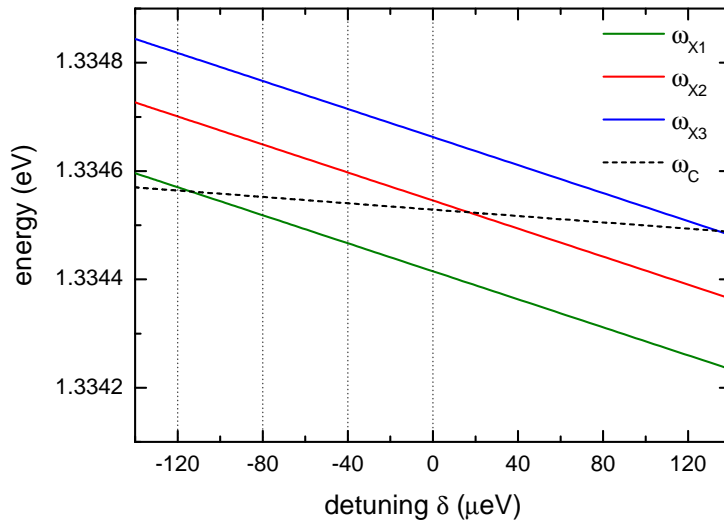


FIG. S4. Energies of the uncoupled QD-exciton and cavity modes as function of the detuning  $\delta = \omega_C - (\sum_{n=1}^3 g_n \omega_{Xn}) / (\sum_{n=1}^3 g_n)$ . Dotted vertical lines correspond to the values of the detuning used in Fig. S5.

Coherent coupling analysis for  $\delta = -133 \mu\text{eV}$  ( $T = 13.5 \text{ K}$ ) is shown in Fig. S6. (a) 2D FWM diagram  $|P_{\text{cor}}(\omega, \omega_\tau)|^2$  obtained by phase correcting  $P(\omega, \tau)$  at  $\omega_{\text{cor}} = 1334.52 \text{ meV}$  (as marked by the arrow) and Fourier-transforming the corrected data along  $\tau$ . Dash-dotted line represents the diagonal  $\omega = \omega_\tau$ . The 2D FWM response contains both first- and second-rung signals masking the coherent coupling features due to the broad spectral width of second- to first-rung transitions. Theoretical spectra corresponding to (a) are calculated with (b) and without (c) phase correction. In (a-c) linear colour scale over 2 orders of magnitude is used. (d) 2D FWM retrieved by using the signal emitted after a time-lag of 42.5 ps, and the phase correction routine is applied as in (a). In this case the 28 second- to first-rung transitions are virtually suppressed, so that the FWM signal is dominated by the 4 first-rung to ground state transitions. An off-diagonal resonance caused by the cavity mediated coherent coupling of the QDs is detected and well reproduced by the corresponding theoretical simulation, with (e) and without (f) phase correction.

To investigate the nonlinear regime of our measurements, we have performed FWM measurements as function of the excitation power in the pulses  $E_1$  and  $E_2$  at zero delay time  $\tau$ . The resulting FWM spectra and integrated power are shown in Fig. S7. A third order scaling is observed, as expected for the lowest order FWM signal, which is proportional to  $E_1^* E_2^2$ . For higher excitation, the third order scaling saturates, followed by a strong reduction. The total driving power used in the experiment (marked by the vertical line) is within the third-order regime. This implies that polariton levels involved in the FWM experiment are limited to only the first and the second rungs of the TC ladder. We estimate that in the conditions of our experiment each  $E_1$  ( $E_2$ ) pulse delivers 80 (240) photons onto the top facet of the micropillar. This corresponds, in average, to 0.25 (0.75) photons per pulse that are injected into the cavity. With increasing power, a transition to a response dominated by the cavity resonance is observed, resembling a Mollow triplet. We observed an evolution towards a Mollow triplet in a single X-C system<sup>6</sup>. Modeling of the high-excitation response will be reported in a future work.

\* Present Address: Institut für Festkörperphysik, Technische Universität Berlin, Hardenbergstrasse 36, 10623 Berlin, Germany

<sup>1</sup> R. Pässler, E. Griebel, H. Riepl, G. Lautner, S. Bauer, H. Preis, W. Gebhardt, B. Buda, D. J. As, D. Schikora, K. Lischka, K. Papagelis, and S. Ves, *J. Appl. Phys.*, **86**, 4403 (1999).

<sup>2</sup> P. Borri, W. Langbein, U. Woggon, V. Stavarache, D. Reuter, and A. Wieck, *Phys. Rev. B*, **71**, 115328 (2005).

<sup>3</sup> M. Bayer, T. L. Reinecke, F. Weidner, A. Larionov, A. McDonald, and A. Forchel, *Phys. Rev. Lett.*, **86**, 3168 (2001).

<sup>4</sup> B. Patton, W. Langbein, U. Woggon, L. Maingault, and H. Mariette, *Phys. Rev. B*, **73**, 235354 (2006).

<sup>5</sup> S. Seidl, M. Kroner, P. A. Dalgarno, A. Högele, J. M. Smith, M. Ediger, B. D. Gerardot, J. M. Garcia, P. M. Petroff, K. Karrai, and R. J. Warburton, *Phys. Rev. B*, **72**, 195339 (2005).

<sup>6</sup> J. Kasprzak, S. Reitzenstein, E. A. Muljarov, C. Kistner, C. Schneider, M. Strauss, S. Höfling, A. Forchel, and W. Langbein, *Nature Materials*, **9**, 304 (2010).

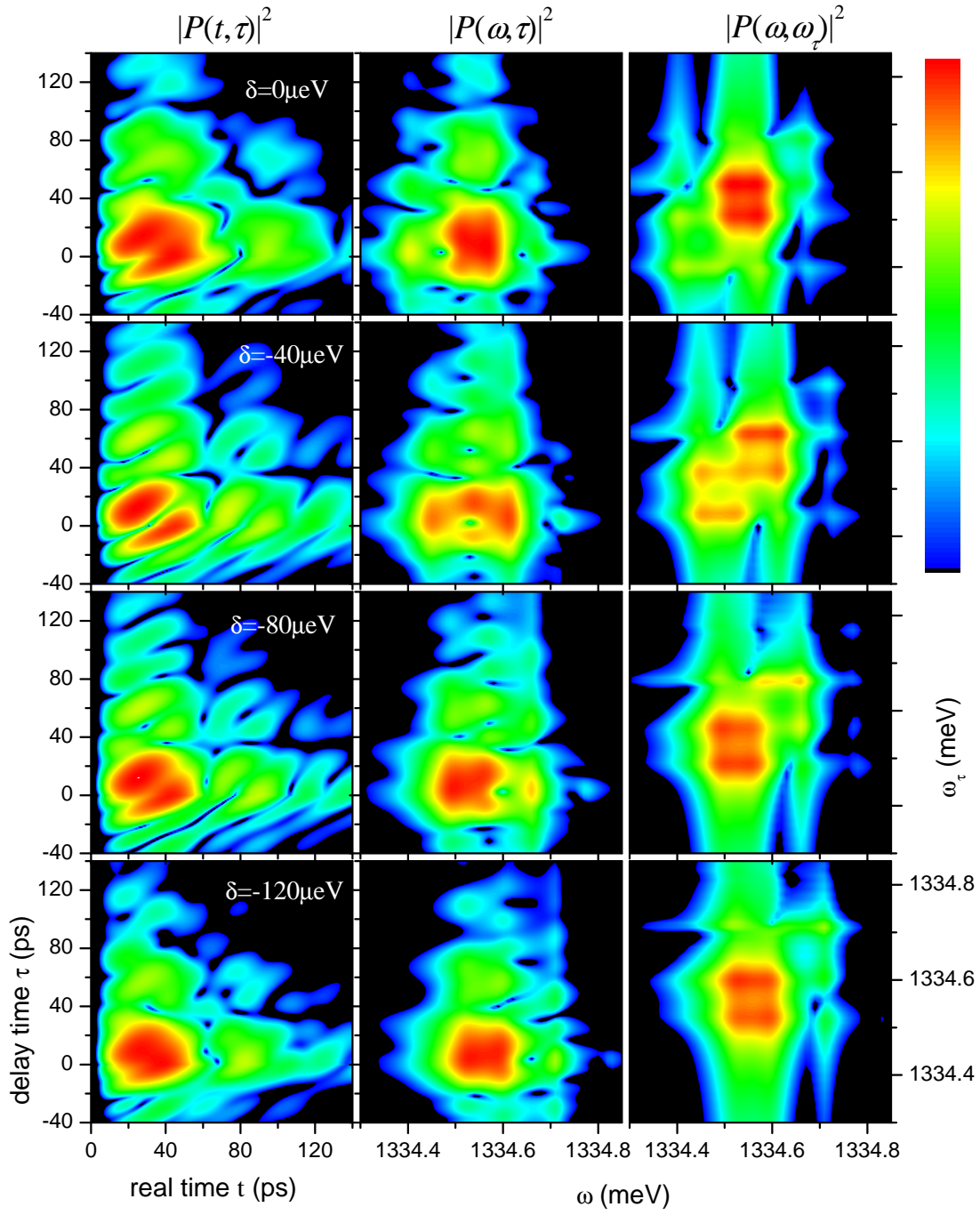


FIG. S5. Calculated FWM versus detuning using the parameters listed in table I. FWM intensities  $|P(t, \tau)|^2$  (left column),  $|P(\omega, \tau)|^2$  (middle column), and  $|P(\omega, \omega_\tau)|^2$  (right column), for the detunings  $\delta = (0, -40, -80, -120) \mu\text{eV}$  from top to bottom. Logarithmic colour scale as shown over 4 orders of magnitude.



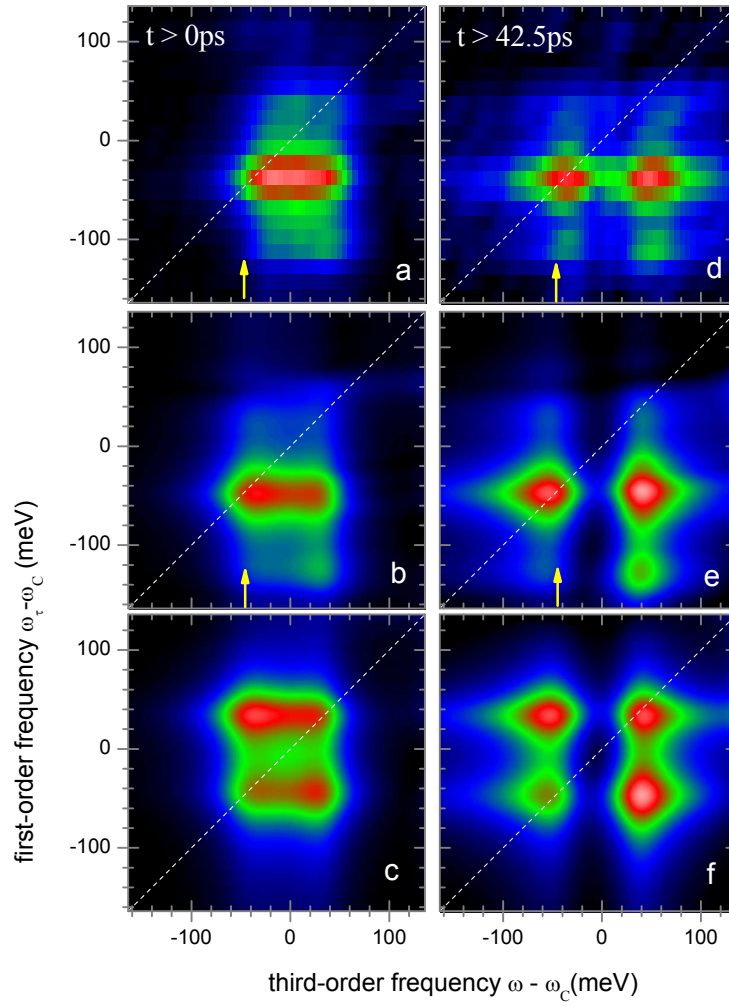


FIG. S6. 2D FWM at  $T = 13.5$  K ( $\delta = -133 \mu\text{eV}$ ). (a)  $|\bar{P}(\omega, \omega_\tau)|^2$ , phase corrected at  $\omega_{\text{cor}} = 1334.52$  meV, marked by the arrow. The diagonal  $\omega = \omega_\tau$  is shown as dashed line. Predicted data corresponding to (a) are shown with (b) and without (c) phase correction. In (a-c) a linear colour scale over 2 orders of magnitude is used. (d) post-selected  $|\bar{P}_s(\omega, \omega_\tau, 42.5 \text{ ps})|^2$ , and its prediction with (e) and without (f) phase correction.

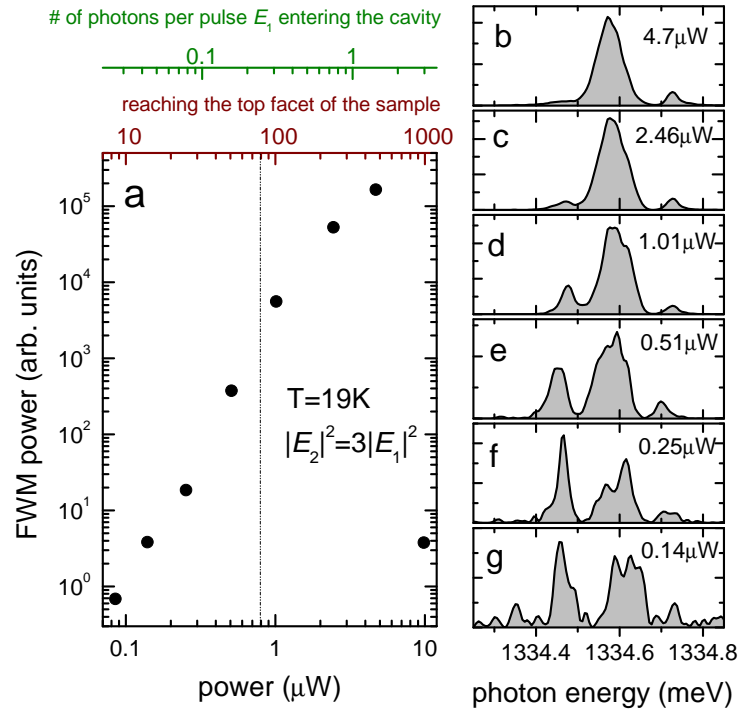


FIG. S7. Intensity dependence of the FWM power. (a) Spectrally integrated FWM power as a function of the combined  $E_1$  and  $E_2$  driving power, at  $\tau = 0$  and  $\delta = -29\mu\text{eV}$  ( $T=19\text{K}$ ). (b-g) Spectrally resolved FWM power for different excitation power as labeled.